Analysis of Long-Term Variation in Spectral Smile of HISUI Using Atmospheric Absorption Bands

Satoru Yamamoto, Satoshi Tsuchida, Minoru Urai, Hiroki Mizuochi, Moe Matsuoka, and Koki Iwao

***Abstract*—This article reports on the long-term variation of the spectral smile and the full-width at half-maximum (FWHM) of the sensor response function for the Hyperspectral Imager Suite (HISUI) onboard the International Space Station (ISS). HISUI is an optical hyperspectral imager comprising two subsystems: a visible-and-near-infrared (VNIR) system covering 400–980 nm and a short-wave infrared (SWIR) system covering 895–2481 nm. On the basis of atmospheric corrections for actual observation images, we found that the characteristics of the spectral smile and the FWHM can be classified into five major periods. The results show that the first two transitions of the periods are due to updates of the smile correction table used in HISUI and that the last one is related to the occurrence of vertical stripes in the HISUI images. However, two unexpected changes are observed. One is a sudden increase in the spectral smile in the SWIR data to 2.0–2.1 nm on September 30, 2021, which was just three days after the second update of the smile correction table. The other is a sudden improvement on January 5, 2022, showing almost zero spectral smile and a nearly constant FWHM. Because neither sudden change is associated with HISUI or ISS operations/events, the optical and electrical systems of HISUI might exhibit instability, leading to sporadic changes of the spectral smile and FWHM. The findings of this study therefore suggest that, although the postlaunch spectral smile correction has been completed, continued long-term evaluation of the spectral stability is important.**

***Index Terms*—Full-width at half-maximum (FWHM), Hyperspectral Imager Suite (HISUI), hyperspectral sensor, response function, spectral smile, wavelength calibration.**

I. Introduction

THE Hyperspectral Imager Suite (HISUI) is a push-broom optical sensor that acquires nadir hyperspectral images covering the 400–980 nm wavelength range at intervals of 10 nm via a visible-and-near-infrared (VNIR) subsystem, and the 895–2481 nm range at 12.5 nm intervals via a short-wave infrared (SWIR) subsystem. The HISUI was developed by Japan's Ministry of Economy, Trade and Industry (METI) [1], [2], [3]. After its launch on December 6, 2019, it was installed in the Japanese Experiment Module (JEM) of the International Space Station (ISS). Following initial checks of the sensor and adjustments to the data processing system on the ISS, data acquisition began on September 4, 2020. The data are recorded on removable media on the ISS, and the media are shipped from the ISS to the ground using a transport spaceship two to three times per year. As of summer 2023, approximately 400 000 scenes have been transported to the ground and processed. In addition, a limited amount of data on the removable media (less than a few GB per day) can be downloaded to the ground using the ISS communication system and the NASA Ku-band immediately after observation acquisition.

The hyperspectral data from HISUI potentially contain a variety of information from discrete absorption and reflection features of the target land surface and the atmosphere. These data are expected to be used in various fields such as environmental monitoring (e.g., plastic materials in coastal areas), vegetation, agriculture, coastal bathymetry, forestry, oil and metal resources, and Earth science [4]. In addition, applications of HISUI data for greenhouse monitoring have also been discussed [5]. In such applications, both an accurate spectral calibration and a radiometric calibration are necessary to extract reliable information from spectral data (see, e.g., [6], [7], [8]). For push-broom-type sensors, in particular, it is important to evaluate and calibrate the spectral smile, which is a phenomenon that results in a cross-track variation in a deviation from the original wavelength assignment because of optical distortion of the light incident on the detector array [9], [10]. A spectral smile has been reported and discussed for various hyperspectral sensors [10], [11], [12], [13], [14], [15], [16], [17], [18], [19], [20], [21], [22]. Note that spectral smile is a different phenomenon from "spectral variability," which is defined as the variation in spectral shape due to target condition, illumination condition, topography, atmospheric effects, and the effects of spectral mixtures in a mixed pixel (e.g., [23]).

The initial analysis of the wavelength calibration for the HISUI was conducted by Yamamoto et al. [24] (we hereafter refer to this work as "Paper I"). They evaluated the spectral smile and the full-width at half-maximum (FWHM) for the HISUI response function on the basis of atmospheric correction using observation images for the ground surface; this atmospheric correction was partly based on the spectral calibration method for several hyperspectral sensors and field spectrometers [12], [13], [14], [25]. Using the data acquired for desert areas, which are expected to be bright, spatially homogeneous, and spectrally stable, and to exhibit little variation in surface elevation, Paper I reported that substantial spectral smile was observed, with

Manuscript received 22 January 2024; accepted 22 February 2024. Date of publication 27 February 2024; date of current version 6 March 2024. This work was supported by the Ministry of Economy, Trade and Industry of Japan. *(Corresponding author: Satoru Yamamoto.)*

Satoru Yamamoto, Satoshi Tsuchida, Hiroki Mizuochi, Moe Matsuoka, and Koki Iwao are with the Geological Survey of Japan, National Institute of Advanced Industrial Science and Technology, Tsukuba 305-8567, Japan (e-mail: yamamoto.satoru@aist.go.jp).

Minoru Urai is with the Geological Survey of Japan, National Institute of Advanced Industrial Science and Technology, Tsukuba 305-8567, Japan, and also with the Japan Space Systems, Tokyo 105-0011, Japan.

Digital Object Identifier 10.1109/JSTARS.2024.3370143

TABLE I
BASIC SPECIFICATIONS OF HISUI

	VNIR	SWIR
Detector	Si CMOS array detector	PV-MCT array detector
†Wavelength range	405.00–975.00 nm	901.02–2474.76 nm
Total number of bands	58	127
Wavelength resolution	10 nm	12.5 nm
Total number of cross-track samples	1024	1000
Nominal cross-track spatial resolution	20 m	
Nominal along-track spatial resolution	31 m	
Nominal observation swath	20 km	
Quantization	12 bits	
Signal-to-noise ratio	$\geq$ 450 at 620 nm	$\geq$ 300 at 2100 nm

†Center wavelength in the specification.

maximum variations of 1.8 nm in the VNIR data and 4.3–4.5 nm in the SWIR data. In addition, the cross-track variation of the FWHM of the HISUI response function (hereafter referred to as "the FWHM variation") was observed with maximum variations of 5.0 nm for the VNIR region and 2.5–3.5 nm for the SWIR region. To correct the spectral smile, a smile correction table in the internal calibration system of the HISUI was updated on September 27, 2021. However, even after the update, a spectral smile with a maximum variation of ∼2.2 nm was still observed in the SWIR data, whereas the profile for the VNIR region was almost flat (within ∼0.3 nm), with a nearly constant FWHM. Therefore, further investigation is needed to improve the 2.2 nm spectral smile in the SWIR region. In addition, it is important to conduct a long-term evaluation of the spectral stability of the HISUI data. Nevertheless, at the time of the analysis of Paper I, the removable media containing the HISUI observation data had not yet arrived on the ground; the evaluation was therefore based on limited data (only seven scenes in total) transmitted from the ISS using the ISS communication system and the NASA Ku-band. As a result, we could not further investigate the cause of the 2.2 nm spectral smile or assess the long-term spectral stability.

Nonetheless, many removable media containing data acquired on various dates in different HISUI observation areas have been transported to the ground and processed using the ground-based calibration system for HISUI data. Thus, a large volume of desert-area data with various observation dates is available.

There are many issues to be solved in the calibration of hyperspectral data, including correction of spectral smile, correction of pixel-to-pixel variations, sensitivity analysis, and the effects of water vapor. Importantly, in order to solve these calibration issues, spectral smiles need to be removed first, and this article is positioned as the first important calibration step. To this end, the long-term variation of the spectral smile of the HISUI is evaluated in this study on the basis of the atmospheric correction method used in Paper I.

The rest of this article is organized as follows. We first give a brief overview of the HISUI and the data processing in Section II, and the procedure for the atmospheric correction method used in Paper I in Section III. We then evaluate the spectral smile and the FWHM for the VNIR and SWIR data over various observation dates in Section IV. In Section V, we discuss the long-term variation of both the HISUI spectral smile and the FWHM. Finally, Section VI concludes this article.

II. OVERVIEW OF HISUI AND DATA PROCESSING

Because detailed information regarding the HISUI is given in [1], [2], and [24], the HISUI specifications, particularly those related to the spectral smile and FWHM determination methods, are only briefly summarized here. The HISUI is a push-broom-type imager that comprises two subsystems: VNIR and SWIR detectors. The specifications of these two detectors are summarized in Table I (see also [1]). The VNIR detector is a 1024 × 256-pixel back-illuminated Si complementary metal-oxide-semiconductor (CMOS) array detector with a pixel size of 30 μm ×30 μm. The SWIR detector is a 1000 × 256-pixel photovoltaic mercury cadmium telluride (PV-MCT) array detector with a pixel size of 30 μm ×30 μm; it is thermometrically controlled by a Stirling-type cryocooler. Each VNIR pixel covers a wavelength range of 2.5 nm, and each SWIR pixel covers 6.25 nm.

The data from the detectors are transmitted to the Hyper Electronics Unit (HELU) in the HISUI after 12-b analog-to-digital conversion. To improve the data, the HELU conducts radiometric corrections of photoresponse nonuniformity, nonlinearity, and offsets, as well as correction of spectral smile [1]. In the internal data processing of the HISUI, multiple pixels in the wavelength direction are binned as "one band" in the normal observation mode. In this case, four pixels are binned as one band with a spectral resolution of 10 nm for the VNIR region, and two pixels are binned as one band with a spectral resolution of 12.5 nm for the SWIR region. Because the first four and last two bands of the VNIR region and the first band of the SWIR region are out of specification, 58 out of 64 bands in the VNIR detector and 127 out of 128 bands in the SWIR detector are used. As a result, the VNIR detector covers the wavelength range 400–980 nm and the SWIR detector covers the range 895–2481 nm.

In the internal data processing of the HISUI, the spectral smile is digitally corrected using the binning process, where the contribution from each pixel is calculated using weighted coefficients. For the VNIR detector, the signal $\bar{S}_{\mathrm{v}}(i)$ after binning is obtained as

$$\bar{S}_{\mathrm{v}}(i) = \sum_{k=0}^{5} c_k(i) S(n(i)+k) \tag{1}$$

where $S(n(i)+k)$ is the original signal at a spectral pixel of $n(i)+k$, $n(i)$ is the starting pixel for band i, and $c_k(i)$ are the

weighted coefficients. Notably, the actual $\bar{S}_{\mathrm{v}}(i)$ is a function of a cross-track sample x_{s} in an image; however, the description of x_{s} is omitted here for simplicity of explanation. In (1), the value of k is used from 0 to 5, whereas the original specification requires four pixels to be binned as a single band. If there is no wavelength shift and the wavelength coverage from the incident light on the detector array coincides with that of the original four-pixel allocation, the binning process needs only the four pixels. However, in the case of wavelength shift, the binning process needs to take into account the signals of the two pixels on the left and right in addition to the four pixels. This is why the actual binning process uses six pixels for the VNIR region, and four pixels for the SWIR region.

The weighted coefficients $c_k(i)$ are normalized as

$$\sum_{k=0}^{5} c_k(i) = 1. \tag{2}$$

The values of $c_k(i)$ are determined to track the center wavelength so that wavelength shift is corrected. The simplest situation is a normal binning process with no wavelength shift, with $c_0(i) = c_5(i) = 0$, and $c_1(i) = c_2(i) = c_3(i) = c_4(i) = 1/4$. By contrast, in the case of wavelength shift, signals from six spectral pixels are binned as one band, where the values of $c_k(i)$ are calculated such that the wavelength shift is corrected. For the SWIR data, the signal $\bar{S}_{\mathrm{s}}(i)$ after binning is obtained as

$$\bar{S}_{\mathrm{s}}(i) = \sum_{k=0}^{3} c_k(i) S(n(i) + k). \tag{3}$$

The simplest situation is a normal binning process with no wavelength shift, where $c_0(i) = c_3(i) = 0$ and $c_1(i) = c_2(i) = 1/2$. For the situation with wavelength shift, signals from four spectral pixels are binned, where the values of $c_k(i)$ are calculated such that the wavelength shift is corrected. The $c_k(i)$ data are compiled into a smile correction table uploaded from the ground [3]. The HELU performs the spectral smile correction according to the smile correction table. A weighted average of the response functions for four or six pixels determines the response function for one band. As a result, the FWHM in the data after the binning process depends on $c_k(i)$, which is determined on the basis of the spectral smile characteristics. Thus, if there is spectral smile in the HISUI data, the data also show the FWHM variation. However, if the spectral smile is appropriately corrected, the FWHM variation would be corrected.

As mentioned above, the original signals from spectral pixels are irreversibly binned in the onboard processes before being transferred to the ground. This means that spectral smile and FWHM in the HISUI raw data cannot be corrected on the ground, which is different to e.g., DESIS [21]. The smile properties and FWHM of the HISUI data can only be corrected by the smile correction table uploaded to HISUI. Thus, only the HISUI data obtained after applying the appropriate smile correction table are properly corrected for spectral smile and FWHM.

The data after these corrections in the HELU are transmitted to the mission data processor, followed by recording to removable media on the ISS. The removable media are shipped from the ISS to the ground using a transport spaceship two to three times per year. The raw data (Level 0 data) in removable media transported to the ground are processed to Level 1 A (L1A) data, which are then converted to Level 1R (L1R) data and Level 1 G (L1G) data in the data processing systems on the ground. Table II provides a summary of each data level.

TABLE II
HISUI DATA PRODUCT

Name (abbreviation)	Description
Level 0 (L0)	Raw data not in image format
Level 1A (L1A)	Raw digital number image
Level 1R (L1R)	Radiance image
Level 1G (L1G)	Geometrically corrected radiance image

For redundancy, there are duplicated processing systems on the ground. One of these systems is the HISUI Ground Data System (GDS), which is operated and managed by Japan Space Systems [4]; the other is the Calibration Data Archive System (CDAS), located at the Geological Survey of Japan, National Institute of Advanced Industrial Science and Technology [26]. The GDS and CDAS use essentially the same processing protocols, although they have different data use objectives. The GDS generates L1A, L1R, and L1G data for general users, and archived HISUI products are available for distribution to the public (see [4]). Conversely, the CDAS is a ground data processing and archive system for calibration of the HISUI data; it maintains a radiometric and geometric database that is a collection of calibration parameters used in the GDS. In this study, we used the data in the CDAS.

Preflight tests of the flight model were conducted to investigate the radiometric and spectral properties of the HISUI using the HISUI onboard calibration system (hereafter, "onboard lamps"), consisting of two halogen lamps and a filter wheel with wavelength calibration [1], [2]. During these tests, the spectral smile characteristics were evaluated using the onboard lamps. In addition, the postlaunch evaluation of spectral smile was conducted based on the data obtained using the onboard lamps [3]. However, Paper I revealed that the path of light from the onboard lamps is not exactly the same as that through the full optical system of the HISUI instrument and that, as a result, the correction based on the analysis using the onboard lamps causes a "false spectral smile" in the actual observation images. Thus, we did not use the data obtained using the onboard lamps to evaluate the spectral smile and the FWHM (see [24] for further details).

Finally, we note some of the observational limitations inherent to the ISS. Because the ISS is not in a Sun-synchronous orbit, 1) the observation local time is not constant; 2) the solar elevation changes substantially from observation to observation; and 3) the HISUI observations are performed in both a descending and ascending orbits. In addition, the attitude of the ISS is always unstable; thus, the target areas are not always observed as planned. These situations limit the data available for analysis in this study, especially for the data intervals that can be used to assess long-term variation of the spectral smile and the FWHM.

TABLE III
ATMOSPHERIC MOLECULAR BANDS USED IN THIS STUDY AND THE WAVELENGTH RANGE FOR THE CALCULATION OF C_i

Band name	Representative center wavelength [nm]	Molecular species	VNIR or SWIR	Beginning λ corresponding to $i_{\min}$ [nm]	End λ corresponding to $i_{\max}$ [nm]
Band V1	765	O_2	VNIR	745.0	785.0
Band S1	1260	O_2	SWIR	1238.2	1288.2
Band S2	2010	CO_2	SWIR	1987.6	2037.6
Band S3	2060	CO_2	SWIR	2037.6	2087.6

III. METHOD

A. Atmospheric Correction Method

To evaluate the wavelength shift $\delta\lambda$ from its original wavelength assignment, we use the atmospheric correction method applied in Paper I. This method uses the major molecular absorption bands of the Earth's atmosphere to estimate $\delta\lambda$ from a comparison of the radiance between an actual observation (a measured radiance) and a model calculated with MODTRAN (a model radiance).

The characteristics of spectral smile are then assessed from how $\delta\lambda$ depends on x_s in an image. This method also enables us to evaluate the FWHM, W_{FM}, of each spectral band of the sensor (see [22] and [27]). The detailed analytical procedure is given in Paper I; we therefore give only a brief explanation here.

Table III lists the absorption bands used in the atmospheric correction method. Absorption bands of H_2O are not used here because each H_2O absorption band is too wide for the center wavelength to be accurately determined in the wavelength range of 1 nm or less. Using MODTRAN 6, we calculated a modeled radiance incident on HISUI from the target site, where the Gaussian model is used to characterize the spectral response function of each spectral band of the HISUI sensor. As representative parameter values for MODTRAN calculations, we used 1) the U.S. Standard 1976 Atmospheric Profile; 2) the desert aerosol model; 3) a Lambertian desert-barren surface type. In addition, target latitude and longitude, ground height, solar altitude, and seasonal parameters were used for each target and observation timing. Before determining $\delta\lambda$ and W_{FM} for each scene, the amounts of O_2 and CO_2 are first adjusted so that the depths of the absorption bands due to O_2 and CO_2 in a modeled radiance are close to those in a measured radiance. The values obtained are applied to all pixels in each scene. Notably, the aim of this study is not to determine the exact surface reflectance but to estimate $\delta\lambda$ for a large number of pixels in various HISUI scenes. Thus, instead of fine-tuning MODTRAN parameters for each pixel, we used the simple and efficient method described above. Consequently, the ratio of a measured radiance to a modeled radiance (hereafter, "the radiance ratio") is not exactly unity in the figures presented below.

Fig. 1(a) shows a comparison of the measured radiance and the modeled radiance in the SWIR region, where an absorption feature in Band S1 (due to O_2 absorption) is observed at $1240 \leq \lambda \leq 1280$ nm. We then calculated the ratio of the measured radiance shifted by a wavelength of ω to the modeled radiance, as shown in Fig. 1(b), where the shifted data were obtained using a cubic spline interpolation according to the method used in [28]. For the case of $\omega = -1.00, -2.00, -4.00$, and -5.00 nm, a concave or convex feature in the wavelength range $1240 \leq \lambda \leq 1280$ nm is observed in the radiance ratio, indicating that the shape of Band S1 for the measured radiance is not consistent with that for the modeled radiance. However, the radiance ratio with $\omega = -3.00$ nm is a nearly flat feature at $1240 \leq \lambda \leq 1280$ nm, indicating that the shape of Band S1 in the measured radiance well matches that of the modeled radiance. As such, we can estimate ω by searching for a nearly flat feature in the radiance ratio. In addition, because the shape of the radiance ratio depends on W_{FM}, we can determine the best solution for W_{FM} by searching for a nearly flat feature in the radiance ratio among the results with various W_{FM}. Thus, when the optimal solution is obtained by performing a grid search for the parameter space of ω and W_{FM}, we can estimate the wavelength shift $\delta\lambda = -\omega$.

To determine the best solution for ω and W_{FM}, we use the root mean square (rms) value χ

$$\chi = \sqrt{\sum_{i=i_{\min}}^{i_{\max}} (R_i - C_i)^2} \tag{4}$$

where R_i is the radiance ratio, the subscript i indicates the band number, and the continuum C_i is calculated by linear fitting to the data points at $i = i_{\min}$ to $i_{\max}$ for R_i. Since the current HISUI data are still affected by the influence of H_2O and various artifacts such as pixel-to-pixel variations and noise components due to insufficient radiometric calibration, we adopt (4) to evaluate the best solution for ω and W_{FM}, rather than advanced mathematical methods such as the maximum cross-correction method. Wavelength ranges that correspond to $i_{\min}$ and $i_{\max}$ for Bands V1, S1, S2, and S3 are listed in Table III. Note that there are absorption bands of H_2O before and after each of the O_2 and CO_2 bands used in the analysis. Since the amount of H_2O can vary significantly from pixel to pixel owing to local variations in atmospheric conditions, the wavelength coverage between $i_{\min}$ and $i_{\min}$ should be set to avoid the influence of H_2O. In each of the O_2 and CO_2 bands, the wavelength range unaffected by H_2O is limited (up to ~40–60 nm), and thus we cannot extend the wavelength range used in Table III. In addition, a narrower wavelength range than the current value does not adequately cover each of the O_2 and CO_2 bands. Thus, the values of $i_{\min}$ and $i_{\max}$ in Table III are the most optimal ones.

We calculated χ for various values of ω and W_{FM} and performed a grid search to obtain the optimal solution of these parameters. The search range for ω was set to -7.0 to 7.0 nm with an increment of 0.1 nm, and that for the standard deviation σ ($W_{\mathrm{FM}} = 2\sigma\sqrt{2\ln 2}$) for the Gaussian model was set

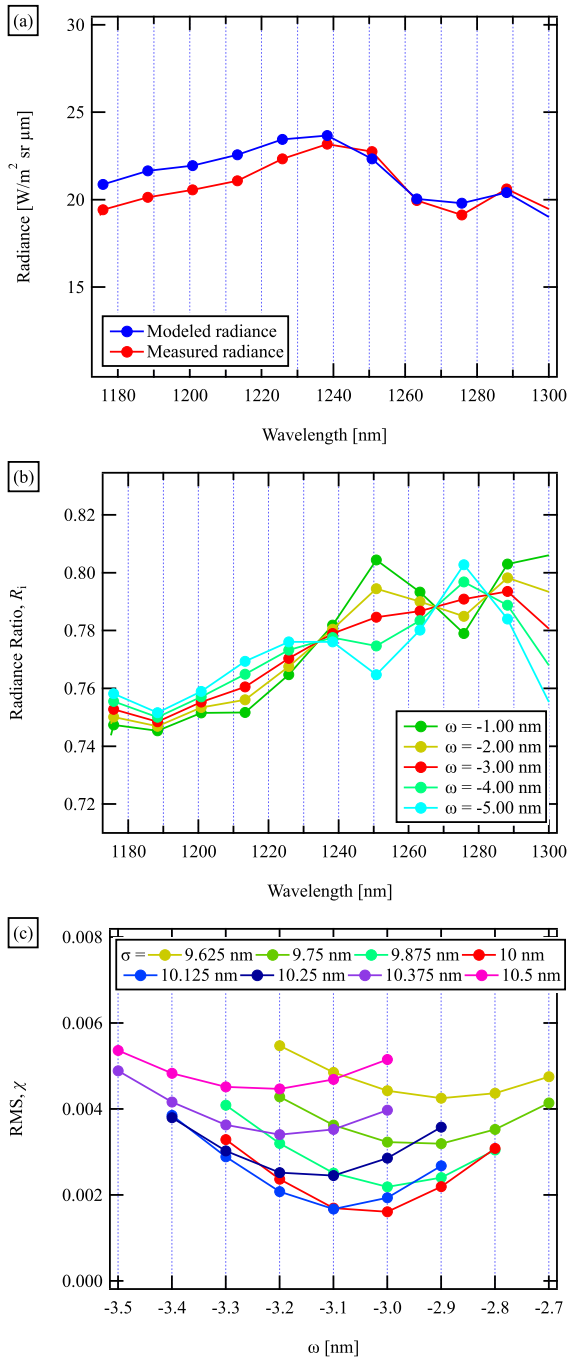

Fig. 1. (a) Radiance measured (red circles) by the HISUI for a desert region and modeled radiance (blue circles) convolved with a Gaussian model with $W_{\mathrm{FM}} = 23.55$ nm. A broad depression in the wavelength range $1240 \leq \lambda \leq 1280$ nm for both the measured and modeled radiances is due to an O_2 absorption (Band S1). Here, we used $\omega = 0.0$ nm for the measured radiance. (b) Radiance ratios using the data in (a) for various ω. (c) rms χ for Band S1 plotted against ω for various σ ($W_{\mathrm{FM}} = 2\sigma\sqrt{2\ln 2}$).

to 2.0–15.0 nm with an increment of 0.125 nm. Fig. 1(c) shows the χ values for various ω and W_{FM} for the data in Fig. 1(a). The minimum χ is located at $\sigma = 10.00$ nm ($W_{\mathrm{FM}} = 23.55$ nm) and $\omega = -3.0$ nm, indicating $\delta\lambda = +3.0$ nm. Note that the value of W_{FM} in a modeled radiance is different from the wavelength resolution of 10 nm for VNIR or 12.5 nm for SWIR in Table I. The W_{FM} is a parameter of the Gaussian model used for convolution with data calculated by MODTRAN, whereas the wavelength resolution of 10 or 12.5 nm is used as a parameter to integrate the wavelength range to simulate how each of the HISUI detectors actually measures the light.

B. Data

To assess the spectral smile characteristics in images, L1R data in the normal observation mode were used instead of L1G data. Desert areas were selected as target sites because they were expected to be bright, spatially homogeneous and spectrally stable, and to exhibit little variation in surface elevation. As described above, the timing, location, and occasion of the available observation data are sometimes biased because of the observational limitations inherent to the ISS. Therefore, the data used for long-term monitoring had to be discrete during several periods. Table IV summarizes the observation ID, dates, observation sites with the latitude and longitude of the center point of an image, altitude, and the solar elevation for the data used in this study.

Note that the Radiometric Calibration Network (RadCalNet [29]) and pseudoinvariant calibration sites (PICS [30]) can be useful for the evaluation of spectral smile, because these sites provide the information about ground surface reflectance, atmospheric parameters, spatial homogeneity, and spectral stability. Indeed, these sites are set as one of the most important areas of interest (AOI) in the HISUI calibration plan. However, there are few opportunities to observe these sites, because the ISS orbit is not in a sun-synchronous, and is always unstable and irregular. In addition, the attitude of the ISS is always unstable, and thus the target areas are not always observed as planned, even if there is an opportunity to observe these sites. As a result, no sufficient data for RadCalNet or PICS observation sites are available for the evaluation of long-term spectral stability.

IV. Results

In the following, we first show an example of the procedure for evaluating the spectral smile and FWHM for the ID 211202 data in Section IV-A. Next, we show the long-term variation of spectral smile. However, vertical stripes were observed in the images acquired after April 1, 2022, indicating that the optical properties of the HISUI might have changed. Therefore, the results are presented separately for data corresponding to the periods before (see Section IV-B) and after (see Section IV-C) the occurrence of vertical stripes. (Note that the vertical stripes are corrected in the public L1 product.)

A. Evaluation of Spectral Smile and FWHM

Fig. 2 shows a color composite image of the VNIR data for ID 211202, where red, green, and blue are assigned to the bands of $\lambda = 725$, 665, and 515 nm, respectively. This is an image of a desert area in Libya; the area is expected to be spatially homogeneous and spectrally stable, and to exhibit little variation in surface elevation. In this analysis, five lines ("Line A" through "Line E") were selected, and the optimal solutions for ω (and

TABLE IV
CONDITIONS OF TARGET AREAS

Observation ID	Date	Target area (country)	†Latitude and longitude	Altitude [km]	Solar elevation angle [deg]
201013	October 13, 2020	Desert (Algeria)	30.257°N, 9.161°E	0.3	30
201029	October 29, 2020	Desert (Algeria)	31.755°N, 8.987°E	0.2	41
201231	December 31, 2020	Desert (Sudan)	16.369°N, 24.636°E	0.7	45
210228	February 28, 2021	Desert (Tunisia)	32.034°N, 9.282°E	0.2	41
210326	March 26, 2021	Desert (Libya)	24.525°N, 21.693°E	0.4	40
210412	April 12, 2021	Desert (Algeria)	30.186°N, 8.927°E	0.3	43
210505	May 5, 2021	Desert (Niger)	17.574°N, 14.664°E	0.5	50
210506	May 6, 2021	Desert (Mali)	18.802°N, 4.076°W	0.3	43
210527	May 27, 2021	Desert (Libya)	27.537°N, 16.289°E	0.6	50
210610	June 10, 2021	Desert (Tunisia)	31.637°N, 8.398°E	0.2	59
210826	August 26, 2021	Desert (Libya)	24.575°N, 20.290°E	0.5	76
210923	September 23, 2021	Desert (Sudan)	15.387°N, 25.950°E	0.8	40
210929	September 29, 2021	Desert (Mauritania)	19.796°N, 6.327°W	0.3	62
210930	September 30, 2021	Desert (Egypt)	23.775°N, 26.611°E	0.6	59
211025	October 25, 2021	Barren (U.S.)	36.220°N, 110.242°W	1.9	41
211028	October 28, 2021	Desert (Libya)	24.536°N, 14.056°E	0.6	51
211202	December 02, 2021	Desert (Libya)	24.417°N, 22.410°E	0.4	43
211228	December 28, 2021	Desert (Sudan)	20.399°N, 26.496°E	0.6	45
220103	January 3, 2022	Desert (Somalia)	7.737°N, 49.043°E	0.5	43
220104	January 4, 2022	Desert (Australia)	29.637°S, 131.863°E	0.2	79
220105	January 5, 2022	Desert (Namibia)	24.997°S, 15.302°E	0.7	70
220106	January 6, 2022	Desert (Australia)	21.413°S, 136.111°E	0.3	63
220115	January 15, 2022	Desert (Namibia)	25.978°S, 15.443°E	0.7	42
220129	January 29, 2022	Desert (Libya)	24.677°N, 20.985°E	0.4	46
220202	February 2, 2022	Desert (Libya)	25.075°N, 21.912°E	0.3	47
220218	February 18, 2022	Desert (Libya)	24.106°N, 12.885°E	0.7	43
220302	March 2, 2022	Desert (Mauritania)	20.922°N, 6.195°W	0.3	45
220328	March 28, 2022	Desert (Libya)	32.429°N, 6.699°E	0.7	44
220329	March 29, 2022	Desert (Libya)	20.993°N, 24.946°E	0.7	63
220401	April 1, 2022	Desert (Chad)	16.934°N, 16.083°E	0.2	78
220405	April 5, 2022	Desert (Tunisia)	32.991°N, 8.538°E	0.1	62

†Latitude and longitude at representative center point of VNIR image.

$\delta\lambda$) and W_{FM} were obtained at every 20 cross-track samples along x_{s} (black "+" symbols). In Fig. 3(a), $\delta\lambda$ for Band V1 is plotted against x_{s}, where the red curve is the average of the five different lines. All the data exhibit a nearly constant $\delta\lambda$ between approximately -3.5 and -3.0 nm. Indeed, quadratic and cubic curve fittings resulted in maximum differences of $\sim$0.30 and $\sim$0.35 nm, respectively. These results indicate that the maximum cross-track variation in $\delta\lambda$ for the average value due to spectral smile is $\Delta\lambda_{\max}\sim$0.35 nm. In addition, the typical difference between the average and each line is less than $\sim$0.1 nm, indicating that there is no significant difference in $\delta\lambda$ among the five lines. In Fig. 3(b), W_{FM} for Band V1 is plotted against x_{s}, where W_{FM} exhibits an almost constant value between 16.5 and 17.0 nm. In addition, the typical difference between the average and each line is less than $\sim$0.2 nm.

We similarly evaluate $\delta\lambda$ and W_{FM} for the SWIR data. In Fig. 4(a), the average values of $\delta\lambda$ for Bands S1, S2, and S3 are plotted against x_{s}. In contrast to Band V1, all the overall trends exhibit a substantial quadratic curve (spectral smile) with x_{s}. For Band S1, $\delta\lambda$ in the range $400 \leq x_{\mathrm{s}} \leq 600$ is 5.4 nm and $\delta\lambda$ at the ends of x_{s} is $\sim$4.1 nm (left end) and $\sim$3.3 nm (right end). Thus, we estimate $\Delta\lambda_{\max}\sim$2.1 nm for Band S1. For Bands S2 and S3, the maximum value of $\delta\lambda$ is 4.7–4.8 nm in the range $300 \leq x_{\mathrm{s}} \leq 500$ and $\delta\lambda$ at the ends of x_{s} is 4.0–4.1 nm (left end) and 2.8 nm (right end). Thus, we estimate that $1.9 \leq \Delta\lambda_{\max} \leq 2.0$ nm for Bands S2 and S3. In Fig. 4(b), the average values of W_{FM} for Bands S1, S2, and S3 are plotted against x_{s}. The overall shape is similar for Bands S1, S2, and S3, where each W_{FM} becomes a minimum at $500 \leq x_{\mathrm{s}} \leq 600$ and increases at both ends of x_{s}. From Fig. 4(b), the maximum variations in W_{FM} are estimated to be approximately 2.9 nm (Band S1), 2.6 nm (Band S2), and 3.5 nm (Band S3), respectively.

B. Long-Term Variation of Spectral Smile Before April 2022

We next investigate the long-term variation of spectral smile using the above methods.

1) VNIR: Fig. 5(a) shows the long-term variation of $\delta\lambda$ for Band V1, where the range of variation of $\delta\lambda$ for each data point is plotted as maximum and minimum error bars. A slight variation is observed in the maximum and minimum values among the data, which might be due to uncertainties in the determination of $\delta\lambda$ by the atmospheric correction method (refer to Paper I). Notably, the value of $\delta\lambda$ changes discontinuously at certain timings (vertical dotted lines in Fig. 5). From the discontinuous changes, we can identify four different periods: Period 1 (P1) before May 6, 2021, Period 2 (P2) from May 27, 2021 to September 23, 2021, Period 3 (P3) from September 29, 2021 to January 4, 2022, and Period 4 (P4) from January 5, 2022 to March 29, 2022. We found that some discontinuous changes in $\delta\lambda$ are associated with HISUI operational events. The smile correction table was first updated on May 23–24, 2021, which corresponds to the boundary between P1 and P2. The smile correction table was updated again on September 27,

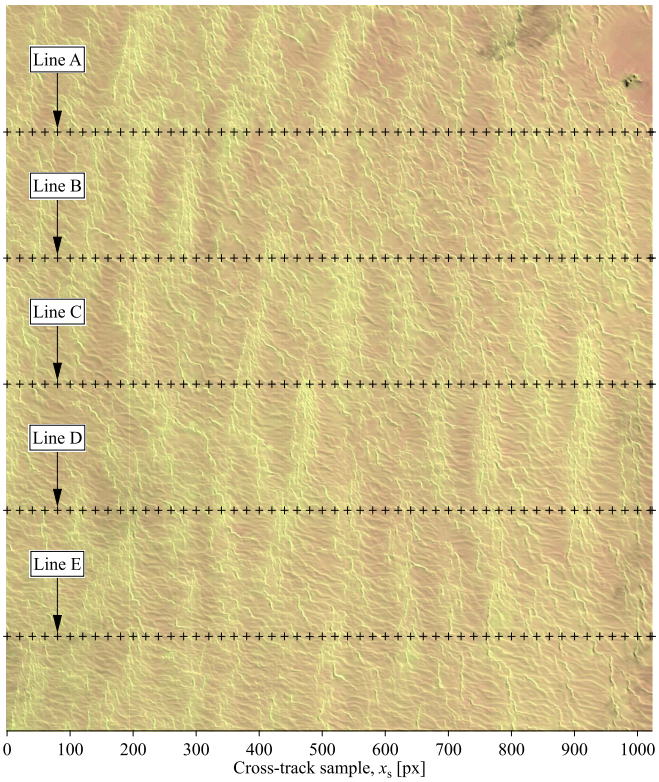

Fig. 2. Color composite image for VNIR data for ID 211202, where red, green, and blue are assigned to bands at 725, 665, and 515 nm, respectively. Black "+" symbols indicate the positions for determining $\delta\lambda$ and W_{FM}.

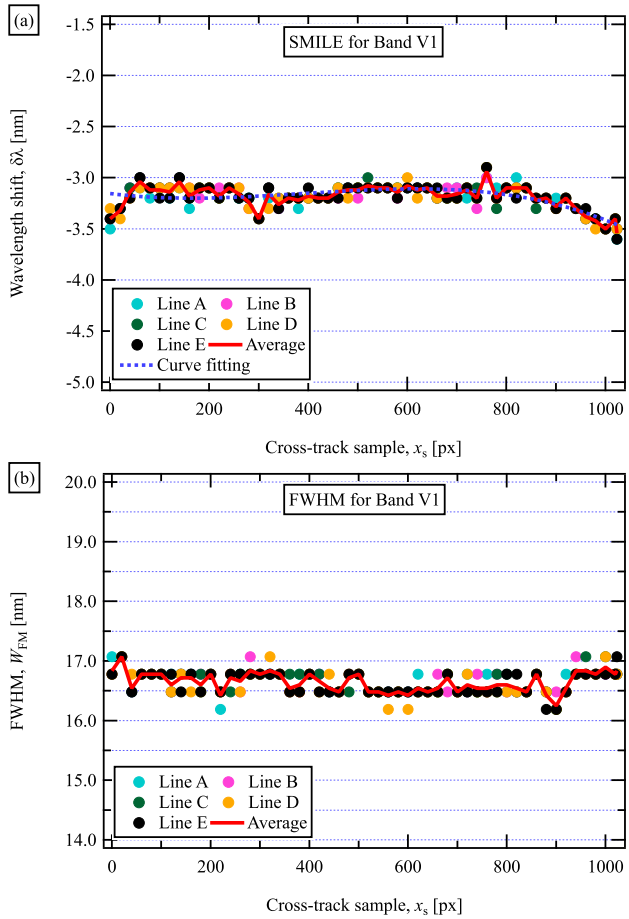

Fig. 3. (a) Wavelength shift, $\delta\lambda$, and (b) FWHM, W_{FM}, for Band V1 for ID 211202, plotted against x_{s}. The blue dotted curve indicates the result of cubic curve fitting.

2021, which corresponds to the boundary between P2 and P3. However, no event between P3 and P4 has thus far been reported, although the range of variation of $\delta\lambda$ dramatically decreases to nearly zero on January 5, 2022.

Fig. 5(b) shows the long-term variation of $\Delta\lambda_{\max}$, which corresponds to the difference between the maximum and minimum values of $\delta\lambda$ in Fig. 5(a). In this case, no clear difference in $\Delta\lambda_{\max}$ is observed between P1 and P2. However, as shown in Fig. 6(a), P1 and P2 have different spectral smile shapes, where the spectral smile for P1 (ID 201029 and ID 201231) shows a nearly trapezoidal shape, whereas that for P2 (ID 210610 and ID 210826) shows a nearly triangular shape. However, both P1 and P2 have similar $\Delta\lambda_{\max}$ of 2.1–2.2 nm because the update of the smile correction table on May 23–24, 2021 corrects mainly the overall wavelength shift. By contrast, as evident in Fig. 6(b), the FWHM variation differs substantially between P1 and P2 because W_{FM} depends on the binning process for multiple pixels and W_{FM} can therefore vary substantially depending on the magnitude of the wavelength shift (refer to Paper I for a detailed explanation).

Note that, as shown in Fig. 5(b), $\Delta\lambda_{\max}$ of the first data point for P3 (September 29, 2021) was almost zero but increased to $\sim$0.3 nm soon afterward. Fig. 6(c) compares $\delta\lambda$ for ID 210929, ID 210930, and ID 211202, where $\delta\lambda$ for ID 210929 is almost constant, with $\Delta\lambda_{\max}\sim$0 nm, indicating that the update of the smile correction table on September 27, 2021 successfully corrected the spectral smile. In addition, Fig. 6(d) shows an almost constant W_{FM} in the data for ID 210929. However, just one day later (ID 210930), a small cross-track variation in $\delta\lambda$ is observed, especially for $x_{\mathrm{s}} < 50$ and $x_{\mathrm{s}} > 900$, with $\Delta\lambda_{\max}$ of approximately 0.3–0.4 nm [see Fig. 6(c)]. A similar cross-track variation of $\delta\lambda$ is also observed in the data for ID 211202. This finding is consistent with Paper I, in which the data obtained on October 2 and 25, 2021 (ID 211002 and ID 211025) were observed to exhibit a cross-track variation of approximately $\pm$0.2 nm. In addition, the results for W_{FM} for ID 210930 and ID 211202 show a large variation compared with those for ID 210929 [see Fig. 6(d)].

The trend of $\delta\lambda$ from September 30, 2021 to January 4, 2022 is approximately the same. However, as shown in Fig. 5(b), the value of $\Delta\lambda_{\max}$ suddenly decreases to near zero on January 5, 2022. This is also evident in Fig. 6(e), where the value of $\delta\lambda$ for ID 220105 is approximately constant with no clear variation, meaning that there is no clear spectral smile in the data. As a result, the cross-track variation in W_{FM} also decreases to $\sim$0.2 nm [see Fig. 6(f)]. However, the data acquired on January 4, 2022 (ID 220104) show a small cross-track variation in both $\Delta\lambda_{\max}$ and W_{FM}.

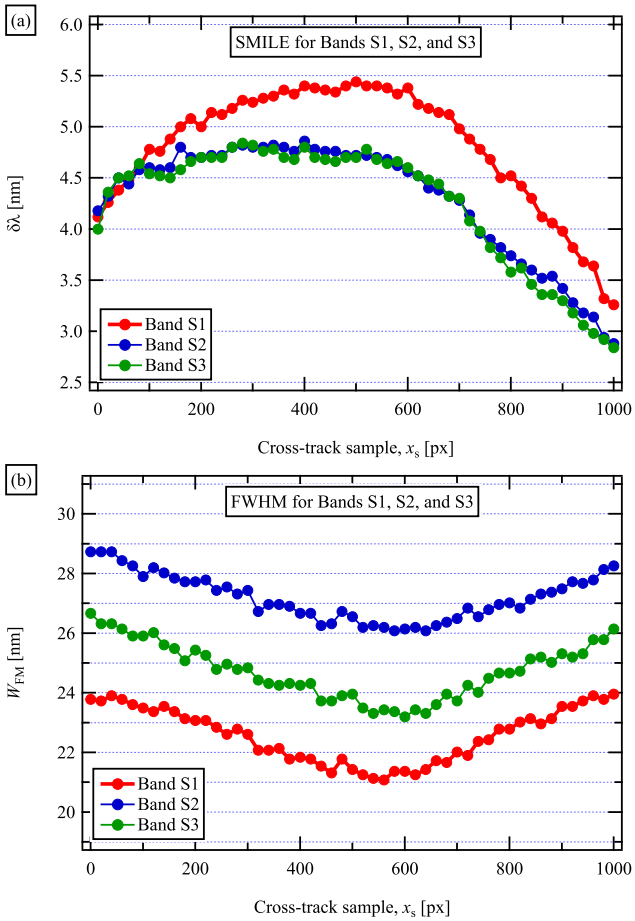

Fig. 4. Average values of (a) $\delta\lambda$ and (b) W_{FM} for Bands S1, S2, and S3 for ID 211202, plotted against x_{s}.

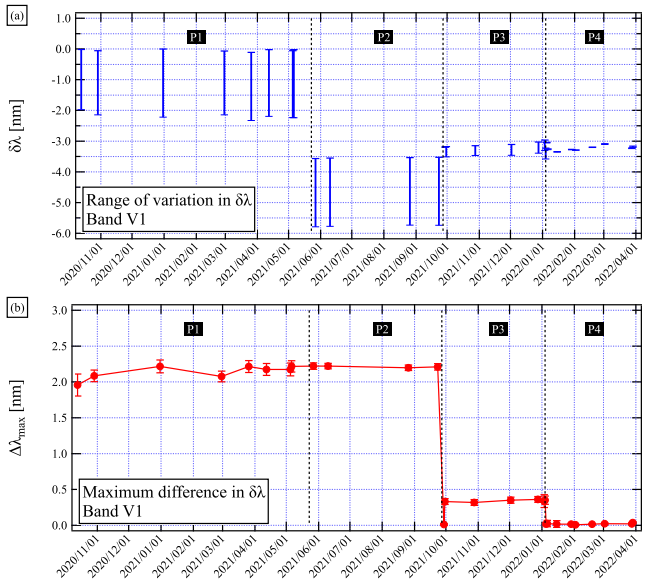

Fig. 5. Long-term variation of (a) $\delta\lambda$ and (b) $\Delta\lambda_{\max}$ for Band V1. Labels in black boxes denote Period 1 (P1), Period 2 (P2), Period 3 (P3), and Period 4 (P4), and the vertical dotted lines correspond to the boundaries between different periods. Here, the boundary between P1 and P2 is set to be the first update of the smile correction table on May 23, 2021.

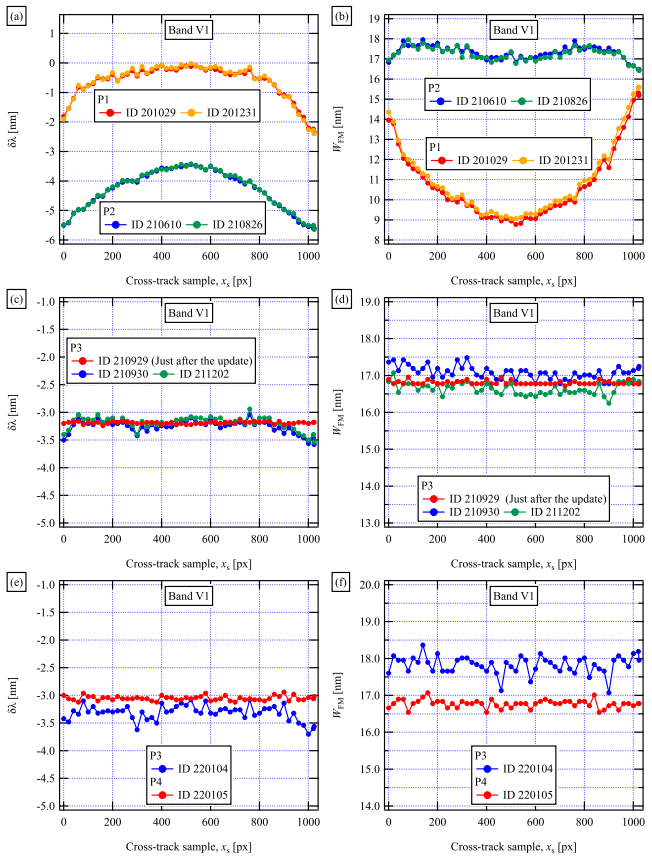

Fig. 6. Comparison of (a) $\delta\lambda$ and (b) W_{FM} for Band V1 between P1 (ID 201029 and ID 201231) and P2 (ID 210610 and ID 210826). (c) and (d) Same as (a) and (b), but for P3 (ID 210929, ID 210930, and ID 211202). (e) and (f) Same as (a) and (b), but for P3 (ID 220104) and P4 (ID 220105).

2) SWIR: Figs. 7 and 8 show long-term variations of $\delta\lambda$ and $\Delta\lambda_{\max}$, respectively, for Bands S1, S2, and S3, with the same period boundaries (vertical dotted lines) as those plotted for the VNIR data. A small difference is observed in $\delta\lambda$ between P1 and P2, where the values of $\delta\lambda$ for P2 are a few tenths of a nanometer larger than those for P1. This difference is more clearly illustrated in Figs. 9(a), 10(a), and 11(a), which compare the shape of the spectral smile between P1 (ID 201029 and ID 201231) and P2 (ID 210610 and ID 210826). These figures show that the overall trend of the spectral smile in P2 is higher than that in P1, whereas the spectral smile shapes in P1 and P2 are similar. In addition, Figs. 9(b), 10(b), and 11(b) show that the values of W_{FM} for P1 and P2 vary substantially with x_{s}, reflecting the large variation of $\delta\lambda$. A folding phenomenon for W_{FM} is observed at $x_{\mathrm{s}} \sim 800$ for Bands S1 and S2 and at $x_{\mathrm{s}} \sim 700$ for Band S3. The folding phenomenon can be seen only in P1 and P2 before the second update of the smile correction table. The smile correction tables used in P1 and P2 were determined based on the ground-based tests, but Paper I revealed that the smile correction tables based on the ground-based tests cause a "false spectral smile" in the actual HISUI data. Thus, the folding phenomenon is digitally generated in the binning process owing to the false spectral smile, resulting in the W_{FM} variation of 6-7 nm, corresponding to a single SWIR pixel of 6.25 nm.

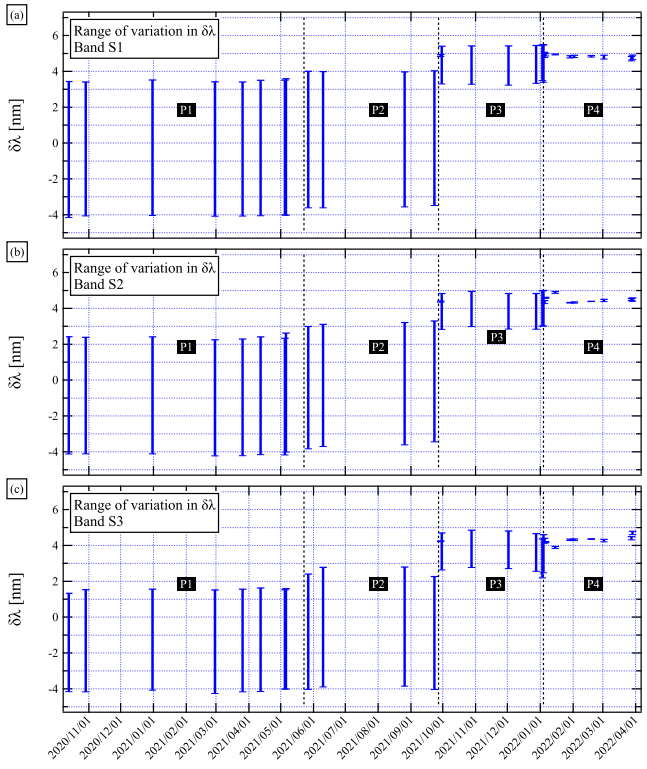

Fig. 7. Long-term variation of $\delta\lambda$ for (a) Band S1, (b) Band S2, and (c) Band S3. Labels in black boxes denote Period 1 (P1), Period 2 (P2), Period 3 (P3), and Period 4 (P4), and the vertical dotted lines correspond to the boundaries between the different periods, which is the same as that in Fig. 5.

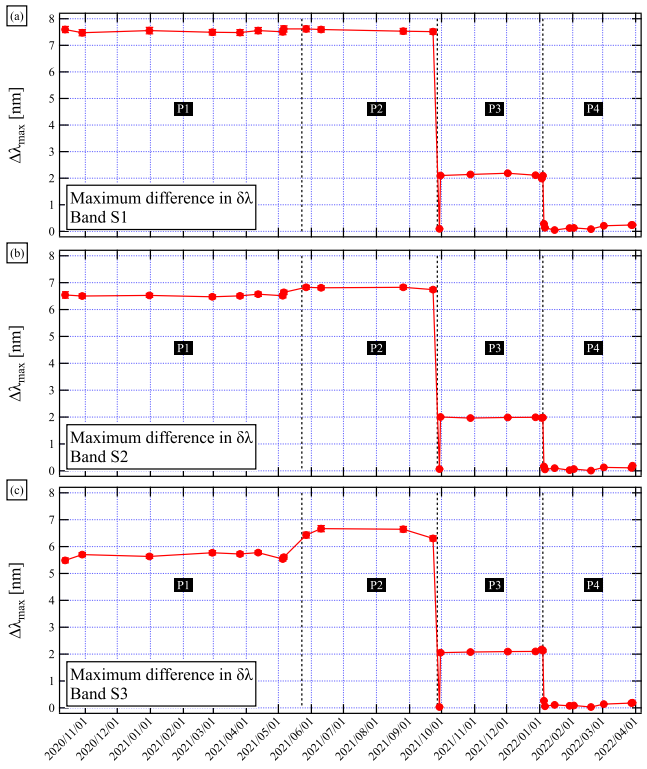

Fig. 8. Same as Fig. 7, but for $\Delta\lambda_{\max}$.

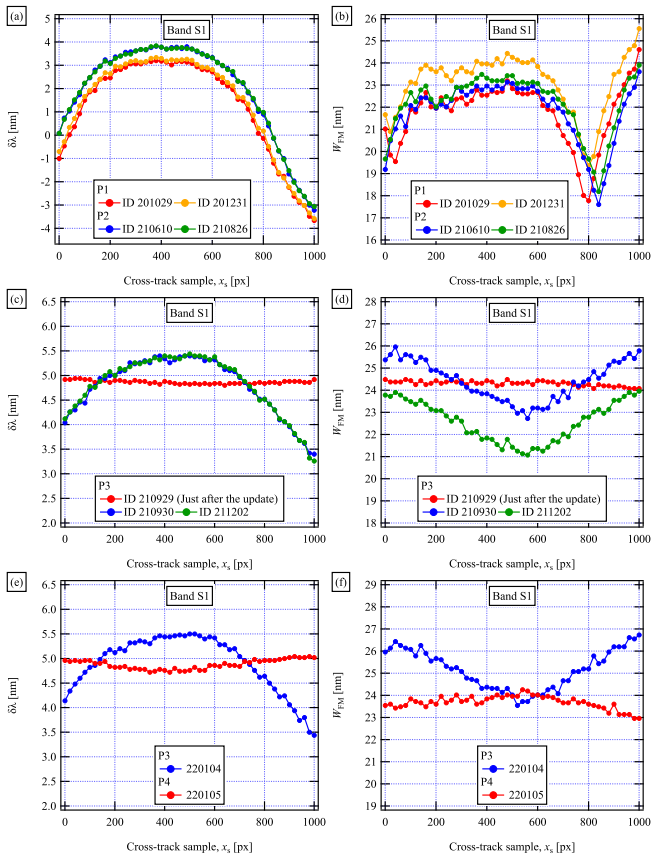

Fig. 9. Comparison of (a) $\delta\lambda$ and (b) W_{FM} for Band S1 between P1 (ID 201029 and ID 201231) and P2 (ID 210610 and ID 210826). (c) and (d) Same as (a) and (b), but for ID 210929, ID 210930, and ID 211202 in P3. (e) and (f) Same as (a) and (b), but for P3 (ID 220104) and P4 (ID 220105).

Returning to Fig. 8, we note that, for the first data point for P3, $\Delta\lambda_{\max}$ improved to almost zero after the second update of the smile correction table but increased to $\sim$2 nm just 1 day later. Indeed, Figs. 9(c), 10(c), and 11(c) show that the results for ID 210929 exhibit a nearly flat $\delta\lambda$, whereas those for ID 210930 and 211202 exhibit clear cross-track variation with $2.1 \leq \Delta\lambda_{\max} \leq 2.2$ nm. In addition, W_{FM} for ID 210929 is approximately flat, whereas those for ID 210930 and 211202 show a cross-track variation of approximately 2.5–3 nm [see Figs. 9(d), 10(d), and 11(d)]. Thus, we confirmed that the second update of the smile correction table once reduced the spectral smile in the SWIR data to almost zero but a spectral smile with $\Delta\lambda_{\max}\sim$2 nm appeared just one day later. This finding is also consistent with the results of Paper I, which showed a cross-track variation of approximately 2.1–2.2 nm for the data obtained on October 2 and 25, 2021.

The spectral smile with $\Delta\lambda_{\max}\sim$2 nm was then observed until January 4, 2022; however, the values of $\Delta\lambda_{\max}$ were found to improve again to near zero on January 5, 2022. This improvement is also evident in Figs. 9(e), 10(e), and 11(e), where $\delta\lambda$ for ID 220105 is nearly flat, indicating no clear spectral smile. Thus, W_{FM} for Bands S1, S2, and S3 exhibits nearly flat

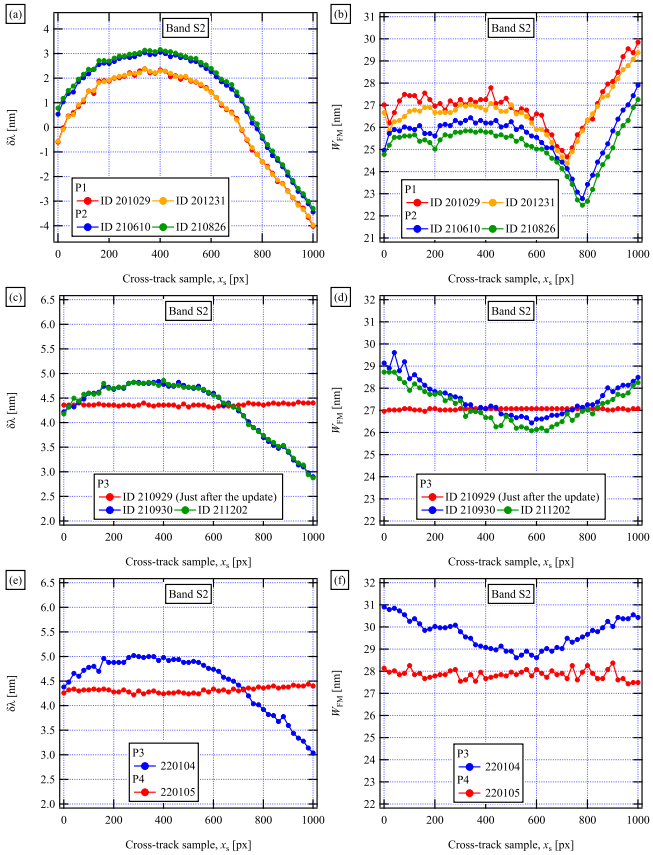

Fig. 10. Same as Fig. 9, but for Band S2.

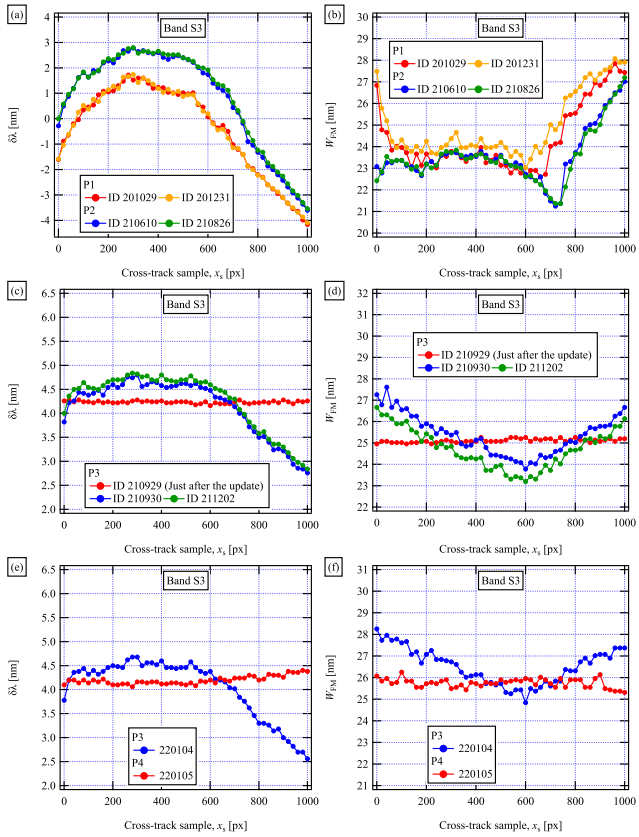

Fig. 11. Same as Fig. 9, but for Band S3.

behavior [see Figs. 9(f), 10(f), and 11(f)]. However, the data for January 4, 2022 (ID 220104) show a clear cross-track variation in both $\Delta\lambda_{\max}$ and W_{FM}.

C. *Spectral Smile After Occurrence of Vertical Stripes*

The appearance of prominent vertical stripes in the HISUI data acquired since April 1, 2022 indicates that the optical properties of the HISUI might have changed. Fig. 12(a) is a color composite image of the VNIR data obtained on April 1, 2022, where prominent vertical stripes are observed in x_{s} ranging from ∼240 to ∼420. Similarly, the SWIR image in Fig. 12(b) shows weak but noticeable vertical stripes in the x_{s} range from 250 to 450. No cause for these stripes has yet been reported, and their origin remains under investigation [4]; however, the timing may be related to an ISS maneuver conducted on March 30, 2022.

While the vertical stripes are corrected in the public HISUI L1 product, investigating how the characteristics of spectral smile and FWHM variation after the occurrence of vertical stripes is important. We therefore analyzed the data for ID 220401 and ID 220405, which are the latest data currently available. Fig. 13 shows $\delta\lambda$ and W_{FM} for Band V1, where the range of x_{s} affected by prominent vertical stripes ($240 \leq x_{\mathrm{s}} \leq 420$) is shaded in gray. The value of $\delta\lambda$ in the shaded region has a variation of approximately 1.1–1.5 nm. However, the overall trend outside the shaded region shows no clear cross-track dependence in $\delta\lambda$ with a variation of ∼0.3 nm, indicating that there is no clear spectral smile in the VNIR data even after the occurrence of the vertical stripes. In addition, as shown in Fig. 13(b), the range of x_{s} outside the shaded region has a nearly constant value of W_{FM} between approximately 16 and 17 nm. Thus, we conclude that the VNIR data except for x_{s} affected by the vertical stripes do not exhibit a significant spectral smile.

Fig. 14 shows $\delta\lambda$ and W_{FM} for Bands S1, S2, and S3 for the data for ID 220401 and ID 220405, where the range of $250 \leq x_{\mathrm{s}} \leq 450$ affected by prominent vertical stripes is shaded in gray. We found that data for x_{s} ranging from approximately 200 to 750 for Band S1 are not available because of saturation of the digital number (DN) of the HISUI data. Fig. 12(b) also shows that the data for x_{s} ranging from approximately 200–750 are brighter than both the regions with $x_{\mathrm{s}} < 200$ and $x_{\mathrm{s}} > 750$, indicating that the distribution of the SWIR radiance data is not homogeneous. Notably, this inhomogeneity is not due to the characteristics of the target surface because we selected a desert area with homogeneous target surfaces. The sensitivity of the SWIR detector might have changed after April 1, 2022.

Returning to the spectral smile characteristics in Fig. 14(a), we note that $\delta\lambda$ for $x_{\mathrm{s}} < 200$ decreases with increasing x_{s} and that $\delta\lambda$ for $x_{\mathrm{s}} > 750$ increases with increasing x_{s}, indicating a cross-track dependence of $\delta\lambda$ for Band S1. Similarly, Fig. 14(c) and (e) also shows a clear cross-track dependence of $\delta\lambda$ both for Bands S2 and S3 with $\Delta\lambda_{\max}$∼2.1 nm. In the shaded region,

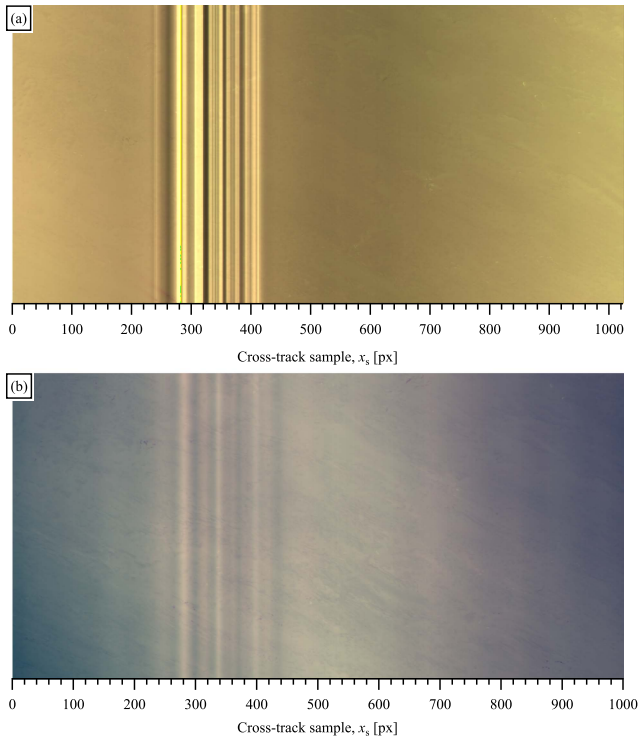

Fig. 12. (a) Color composite image for VNIR data for ID 220401, where red, green, and blue are assigned to bands at 725, 665, and 515 nm, respectively. (b) Same as (a), but for SWIR data, where red, green, and blue are assigned to bands at 1638, 1501, and 1138 nm, respectively.

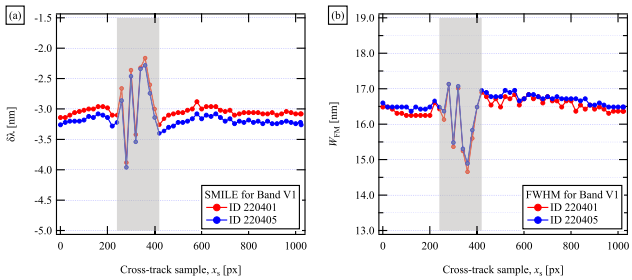

Fig. 13. (a) $\delta\lambda$ and (b) W_{FM} for Band V1 for data obtained after occurrence of vertical stripes in images (ID 220401 and ID 220405). The range of x_{s} affected by prominent vertical stripes is shaded in gray ($240 \leq x_{\mathrm{s}} \leq 420$).

the maximum variation of $\delta\lambda$ is $\sim$1.5 nm, which is less than $\Delta\lambda_{\max}\sim$2.1 nm. However, Fig. 14(d) and (f) shows that there is no clear cross-track dependence of W_{FM} in Bands S2 and S3 within a variation of approximately 0.8–0.9 nm. For Band S1, a small cross-track variation is observed in W_{FM} for $x_{\mathrm{s}} > 750$ [see Fig. 14(b)]; however, determining whether there is a clear cross-track dependence in the overall trend of W_{FM} is difficult. Thus, we conclude that the SWIR data after the occurrence of the vertical stripes exhibit a spectral smile with $\Delta\lambda_{\max}\sim$2.1 nm, whereas W_{FM} shows no clear cross-track dependence, with a variation of approximately 0.8–0.9 nm.

In summary, after the occurrence of vertical stripes, spectral smiles except for the range of x_{s} affected by the vertical

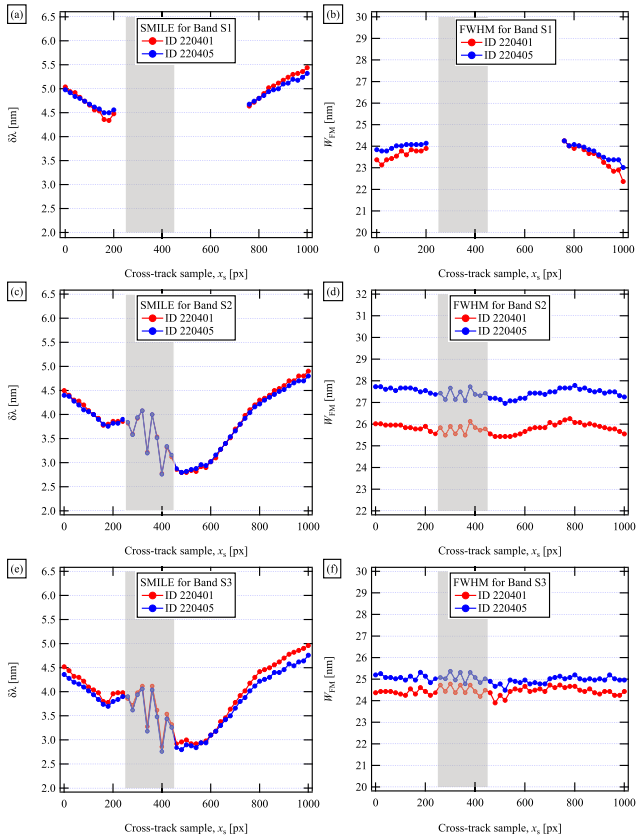

Fig. 14. Values of $\delta\lambda$ and W_{FM} for (a) and (b) Band S1, (c) and (d) Band S2, and (e) and (f) Band S3 for data obtained after occurrence of vertical stripes in images (ID 220401 and ID 220405). The range of x_{s} affected by prominent vertical stripes is shaded in gray ($250 \leq x_{\mathrm{s}} \leq 450$).

stripes increased to $\Delta\lambda_{\max}\sim$0.3 nm in the VNIR data and to $\Delta\lambda_{\max}\sim$2.1 nm in the SWIR data. Interestingly, the extents to which these spectral smiles increased are similar to those in P3.

V. Discussion

A. Summary of Long-Term Variation in Spectral Smile

The above results revealed five periods of change in $\delta\lambda$ and W_{FM} for the HISUI data. Table V summarizes a typical range of $\delta\lambda$, $\Delta\lambda_{\max}$, a typical range of W_{FM}, and the maximum cross-track variation of W_{FM} for each period.

In P1 (before the first update of the smile correction table on May 23–24, 2021), there are substantial spectral smiles with $\Delta\lambda_{\max}$ of 2.1 nm in the VNIR data and 5.7–7.5 nm in the SWIR data; in addition, W_{FM} exhibits irregular cross-track variations of $\sim$6.6 nm in the VNIR data and approximately 4.0–5.6 nm in the SWIR data. After the first update of the smile correction table (P2), the results still show large spectral smiles with $\Delta\lambda_{\max}$ of 2.2 nm in the VNIR data and approximately 6.5–7.6 nm in the SWIR data. In addition, the maximum variation of W_{FM} in the VNIR data is $\sim$1.2 nm, whereas W_{FM} in the SWIR data exhibits irregular cross-track variations of approximately 4.4–5.1 nm. The reason for the remaining spectral smile in both the VNIR and SWIR data even after the first update of the smile correction

TABLE V
SUMMARY OF LONG-TERM VARIATION IN SMILE AND FWHM CHARACTERISTICS

		P1	P2	P3	P4	P5
	Period	†Before 2021/05/23	2021/05/27 to 2021/09/23	‡2021/09/30 to 2022/01/04	2022/01/05 to 2022/03/29	After 2022/04/1
Value	Band					
Typical range of $\delta\lambda$ [nm]	V1	-2.3 to -0.0	-5.8 to -3.5	-3.5 to -3.0	-3.3 to -3.1	-3.4 to -2.9
	S1	-4.1 to 3.5	-3.6 to 4.0	3.2 to 5.5	4.7 to 5.0	NA
	S2	-4.2 to 2.5	-3.8 to 3.3	2.8 to 5.0	4.3 to 4.7	2.8 to 4.9
	S3	-4.2 to 1.6	-4.0 to 2.8	2.3 to 4.8	4.0 to 4.6	2.8 to 5.0
$\Delta\lambda_{\max}$ [nm]	V1	2.1 ± 0.1	2.2 ± 0.01	0.3 ± 0.01	0.02 ± 0.01	0.3 ± 0.03
	S1	7.5 ± 0.1	7.6 ± 0.1	2.1 ± 0.1	0.2 ± 0.1	NA
	S2	6.5 ± 0.1	6.8 ± 0.04	2.0 ± 0.01	0.1 ± 0.1	2.1 ± 0.05
	S3	5.7 ± 0.1	6.5 ± 0.2	2.1 ± 0.04	0.1 ± 0.1	2.1 ± 0.04
Typical range of W_{FM} [nm]	V1	9.0 to 15.9	16.3 to 18.6	16.4 to 18.0	16.1 to 17.5	16.2 to 17.0
	S1	19.1 to 25.7	19.3 to 26.2	21.3 to 27.0	20.1 to 24.5	NA
	S2	24.6 to 30.3	23.2 to 32.6	25.5 to 32.8	25.9 to 30.1	25.4 to 27.8
	S3	22.8 to 28.5	21.8 to 30.5	23.0 to 29.5	23.3 to 26.9	23.9 to 25.3
Maximum cross-track variation of W_{FM} [nm]	V1	6.6 ± 0.1	1.2 ± 0.2	0.5 ± 0.2	0.2 ± 0.3	0.5 ± 0.05
	S1	5.6 ± 0.2	5.1 ± 0.1	2.7 ± 0.1	0.5 ± 0.4	NA
	S2	4.0 ± 0.4	4.4 ± 0.5	2.5 ± 0.1	0.3 ± 0.1	0.8 ± 0.01
	S3	4.5 ± 0.3	4.8 ± 0.2	3.0 ± 0.1	0.4 ± 0.2	0.9 ± 0.01

†The boundary was set to be the first update of the smile correction table. ‡The data for September 29, 2021 were removed.

table is that the main purpose of the first update was to correct the magnitude of the wavelength shift, not the spectral smile. This decision was made because the analysis conducted using the onboard lamps could not reveal the presence of a spectral smile in the HISUI data [3], [24]. On the other hand, the second update of the smile correction table on September 27, 2021 substantially improved the spectral smile in the HISUI data. Indeed, the data acquired on September 29, 2021 show that both the spectral smile and the FWHM variation were almost zero. However, our data also revealed that spectral smiles in both the VNIR and SWIR data increased on September 30, 2021. Consequently, spectral smiles with $\Delta\lambda_{\max}$ of 0.3 nm in the VNIR region and $\Delta\lambda_{\max}$ of 2.0–2.1 nm in the SWIR region were observed in the data acquired from September 30, 2021 to January 4, 2022 (P3). The FWHM also exhibits cross-track variations of $\sim$0.5 nm in the VNIR data and 2.5–3.0 nm in the SWIR data.

Subsequently, the spectral smile and FWHM improved significantly on January 5, 2022. The data from January 5, 2022 to March 29, 2022 (P4) show that spectral smile was nearly zero, with $\Delta\lambda_{\max}$ of 0.02 nm in the VNIR data and $\Delta\lambda_{\max}$ of 0.1–0.2 nm in the SWIR data. W_{FM} is also nearly constant, with small variations of $\sim$0.2 nm in the VNIR data and $\sim$0.3–0.5 nm in the SWIR data. On the other hand, there are small differences in spectral smile and FWHM between bands in P4, which may be due to the inherent spectral smile of the HISUI sensor, because a slight wavelength dependence of a few tenths of a nanometer in the size and shape of the spectral smile was observed in the ground calibration using three solid-state lasers with λ of 1200, 1650, and 1775 nm (see Paper I).

After the occurrence of vertical stripes (P5), the spectral smile slightly increased, with $\Delta\lambda_{\max}$ values of 0.3 nm in the VNIR data and 2.1 nm in the SWIR data, which are similar to the $\Delta\lambda_{\max}$ values in P3. The FWHM also exhibits small cross-track variations of 0.5 nm in the VNIR data and 0.8–0.9 nm in the SWIR data.

The bands available for this analysis are limited to four, because most of the wavelength ranges in the HISUI data are more or less influenced by the H_2O absorption bands. On the other hand, the ground-based calibration using three solid-state lasers showed that the difference of spectral smile due to the wavelength dependence is a few tenths of a nanometer, as mentioned above, and the onboard data after the spectral smile improvement in P4 show the same level of variation, as shown in Table V. Thus, the characteristics of spectral smile and the FWHM obtained from these four bands may be applied to other bands with errors of less than 1 nm.

B. Sudden Changes in Spectral Smile Characteristics of HISUI

Paper I reported that, even after the second update of the smile correction table on September 27, 2021, spectral smile and FWHM variation were still observed in the SWIR data. Paper I suggested that the remaining spectral smile was due to the wavelength dependence of the characteristics of spectral smile and also discussed the possibility that the FWHM for single pixels might be nonuniform in the SWIR data; in this case, the determination of the smile correction table might not fully reflect the actual characteristics of the spectral smile. However, in the present study, we revealed that the spectral smile on September 29, 2021 was nearly zero and that the FWHM was almost constant, indicating that the second update fully improved the spectral smile and the FWHM variation in both the VNIR and SWIR data. The reason for this difference is that only the data acquired in October 2021 was used in Paper I to evaluate the HISUI data after the second update; thus, the improvement on September 29, 2021 was not noticed. In addition, the spectral smile and the FWHM variation in the VNIR and SWIR data improved on January 5, 2022 without an additional update of the smile correction table. These results suggest that the smile functions proposed in Paper I are sufficient to improve spectral smile in the HISUI data. That is, the wavelength dependence of spectral smile and nonuniformity of the FWHM in the SWIR data are not responsible for the remaining spectral smile in the SWIR data.

The reasons for the sudden changes in the spectral smile characteristics on September 30, 2021 and January 5, 2022 are not yet known. This change might indicate that the HISUI optical systems and/or the HISUI electrical data processing systems are sometimes unstable, causing spectral smile to occur sporadically. In addition, the characteristics of spectral smile observed after the occurrence of vertical stripes (P5) are similar to those in P3, which might also be related to such instability. In this case, although the postlaunch spectral smile correction has been completed, continuing further long-term assessments of spectral stability for hyperspectral sensors is important.

VI. Conclusion

We investigated the long-term variation of spectral smile for the HISUI on the basis of the atmospheric correction using actual observation images. The results show that the characteristics of spectral smile and FWHM can be classified into five periods to April 2022, each showing different spectral smile and FWHM characteristics. Two of the boundaries between periods (P1–P2 and P2–P3) correspond to the updates of the smile correction table used in the HISUI, and the P4–P5 boundary is related to the occurrence of vertical stripes in the HISUI images. However, there were also two unexpected changes. The first was a sudden increase in spectral smile to 0.3 nm in the VNIR data and to 2.0–2.1 nm in the SWIR data acquired on September 30, 2021, which was only three days after the second update of the smile correction table that improved the spectral smile and the FWHM variation in the data acquired on September 29, 2021. The other unexpected change was a sudden improvement in the VNIR and SWIR data on January 5, 2022, both of which show almost zero spectral smile and a nearly constant FWHM. We could not identify any event in the operation of the HISUI or the ISS that could cause such sudden changes in the spectral smile and FWHM, possibly indicating that the HISUI optical and electrical systems are sometimes unstable, causing spectral smile to occur sporadically. In addition, the spectral smile characteristics observed after the occurrence of vertical stripes might be related to instability because the spectral smile characteristics in P5 are similar to those in P3. If so, a similar sudden change in the spectral smile characteristics might appear in the future. Thus, although the postlaunch spectral smile correction has been completed, it is important to continue further long-term assessments of spectral stability and to update the smile correction table as necessary.

Finally, we reemphasize that the spectral smile and FWHM in the current HISUI products, especially those before the update of the smile correction table, are not corrected. This is because the HISUI raw data are irreversibly binned in the onboard processes before being transferred to the ground. Using the smile correction table, the spectral smile (and FWHM variation) is digitally corrected in the binning process. This means that the HISUI data obtained after applying (updating) the appropriate smile correction table are corrected for the spectral smile and FWHM, whereas those before the update of the smile correction table have significant spectral smile and FWHM variations as presented in this study. Table V summarizes the spectral smile and FWHM for the HISUI data, which could be useful for users requiring atmospheric correction and reflectance derivation.

Data with the FWHM variation are difficult to use for users who want to perform higher-order analysis using reflectance data with atmospheric corrections. Thus, the FWHM in the cross-track direction needs to be as constant as possible. While it is not easy to reduce the FWHM (increase the wavelength resolution of the data from the current value), it is possible to align the widest FWHM value among the FWHM variations. In this case, a Gaussian blurring function may be used to increase the FWHM of each pixel. In the future, it will be important to consider the production of wavelength-corrected data using a Gaussian blurring function for the HISUI data as an advanced product.

Acknowledgment

The authors would like to thank A. Iwasaki, T. Tachikawa, and Y. Horiguchi for their cooperation in conducting the HISUI project and providing the HISUI data. We would also like to thank the HISUI calibration WG members and those involved in the development of the HISUI.

References

[1] J. Tanii, O. Kashimura, Y. Ito, and A. Iwasaki, "Flight model performances of HISUI hyperspectral sensor onboard ISS (International Space Station)," *Proc. SPIE*, vol. 10423, 2016, Art. no. 104230Q, doi: 10.1117/12.2243846.

[2] A. Iwasaki, J. Tanii, O. Kashimura, and Y. Ito, "Prelaunch status of hyperspectral imager suite (HISUI)," in *Proc. IEEE Int. Geosci. Remote Sens. Symp.*, 2019, pp. 5887–5890, doi: 10.1109/IGARSS.2019.8898660.

[3] M. Urai, S. Tsuchida, S. Yamamoto, T. Tachikawa, A. Iwasaki, and J. Ishii, "Initial onboard calibration results of the HISUI hyperspectral sensor," in *Proc. IEEE Int. Geosci. Remote Sens. Symp.*, 2021, pp. 1608–1610, doi: 10.1109/IGARSS47720.2021.9554224.

[4] HISUI. Accessed: Feb. 29, 2024. [Online]. Available: https://www.jspacesystems.or.jp/en/project/observation/hisui/

[5] T. Matsunaga, S. Yamamoto, and T. Tachikawa, "Detection of large point sources of carbon dioxide by a satellite hyperspectral camera," in *Proc. 7th Workshop Hyperspectral Image Signal Process.: Evol. Remote Sens.*, Tokyo, Japan, 2015, pp. 1–4, doi: 10.1109/WHISPERS.2015.8075481.

[6] R. O. Green, "Spectral calibration requirement for Earth-looking imaging spectrometers in the solar-reflected spectrum," *Appl. Opt.*, vol. 37, no. 4, pp. 683–690, 1998, doi: 10.1364/AO.37.000683.

[7] B.-C. Gao, M. J. Montes, C. O. Davis, and A. F. H. Goetz, "Atmospheric correction algorithms for hyperspectral remote sensing data of land and ocean," *Remote Sens. Environ.*, vol. 113, pp. S17–S24, 2009, doi: 10.1016/j.rse.2007.12.015.

[8] D. R. Thompson, B.-C. Gao, R. O. Green, D. A. Roberts, P. E. Dennison, and S. R. Lundeen, "Atmospheric correction for global mapping spectroscopy: ATREM advances for the HyspIRI preparatory campaign," *Remote Sens. Environ.*, vol. 167, pp. 64–77, 2015, doi: 10.1016/j.rse.2015.02.010.

[9] P. Mouroulis, R. O. Green, and T. G. Chrien, "Design of pushbroom imaging spectrometers for optimum recovery of spectroscopic and spatial information," *Appl. Opt.*, vol. 39, no. 13, pp. 2210–2220, 2000, doi: 10.1364/AO.39.002210.

[10] N. Yokoya, N. Miyamura, and A. Iwasaki, "Preprocessing of hyperspectral imagery with consideration of smile and keystone properties," *Proc. SPIE*, vol. 78570B, 2010, Art. no. 78570B, doi: 10.1117/12.870437.

[11] J. S. Pearlman, P. S. Barry, C. C. Segal, J. Shepanski, D. Beiso, and S. L. Carman, "Hyperion, a space-based imaging spectrometer," *IEEE Trans. Geosci. Remote Sens.*, vol. 41, no. 6, pp. 1160–1173, Jun. 2003, doi: 10.1109/TGRS.2003.815018.

[12] R. O. Green, B. E. Pavri, and T. G. Chrien, "On-orbit radiometric and spectral calibration characteristics of EO-1 hyperion derived with an underflight of AVIRIS and in situ measurements at Salar de Arizaro, Argentina," *IEEE Trans. Geosci. Remote Sens.*, vol. 41, no. 6, pp. 1194–1203, Jun. 2003, doi: 10.1109/TGRS.2003.813204.

[13] B. Cairns, B. E. Carlson, R. Ying, A. A. Lacis, and V. Oinas, "Atmospheric correction and its application to an analysis of hyperion data," *IEEE Int. Geosci. Remote Sens. Symp.*, vol. 41, no. 6, pp. 1232–1244, Jun. 2003, doi: 10.1109/TGRS.2003.813134.
[14] L. Guanter, R. Richter, and J. Moreno, "Spectral calibration of hyperspectral imagery using atmospheric absorption features," *Appl. Opt.*, vol. 45, no. 10, pp. 2360–2370, 2006, doi: 10.1364/AO.45.002360.
[15] B.-C. Gao, M. J. Montes, and C. O. Davis, "Refinement of wavelength calibrations of hyperspectral imaging data using a spectrum-matching technique," *Remote Sens. Environ.*, vol. 90, pp. 424–433, 2004, doi: 10.1016/j.rse.2003.09.002.
[16] A. Dadon, E. Ben-Dor, and A. Karnieli, "Use of derivative calculations and minimum noise fraction transform for detecting and correcting the spectral curvature effect (Smile) in hyperion images," *IEEE Trans. Geosci. Remote Sens.*, vol. 48, no. 6, pp. 2603–2612, Jun. 2010, doi: 10.1109/TGRS.2010.2040391.
[17] K. Staenz, R. A. Neville, S. Clavette, R. Landry, H. P. White, and R. Hitchcock, "Retrieval of surface reflectance from hyperion radiance data," in *Proc. IEEE Int. Geosci. Remote Sens. Symp.*, 2002, pp. 1419–1421, doi: 10.1109/IGARSS.2002.1026135.
[18] B. Datt, T. R. McVicar, T. G. Van Niel, D. L. B. Jupp, and J. S. Pearlman, "Preprocessing EO-1 hyperion hyperspectral data to support the application of agricultural indexes," *IEEE Int. Geosci. Remote Sens. Symp.*, vol. 41, no. 6, pp. 1246–1259, Jun. 2003, doi: 10.1109/TGRS.2003.813206.
[19] L. Guanter, V. Estelles, and J. Moreno, "Spectral calibration and atmospheric correction of ultra-fine spectral and spatial resolution remote sensing data. application to CASI-1500 data," *Remote Sens. Environ.*, vol. 109, pp. 54–65, 2007, doi: 10.1016/j.rse.2006.12.005.
[20] X. Ceamanos and S. Douté, "Spectral smile correction of CRISM/MRO hyperspectral images," *IEEE Trans. Geosci. Remote Sens.*, vol. 48, no. 11, pp. 3951–3959, Nov. 2010, doi: 10.1109/TGRS.2010.2064326.
[21] K. Alonso et al., "Data products, quality and validation of the DLR earth sensing imaging spectrometer (DESIS)," *Sensors*, vol. 19, no. 20, 2019, Art. no. 4471, doi: 10.3390/s19204471.
[22] S. Cogliati et al., "The PRISMA imaging spectroscopy mission: Overview and first performance analysis," *Remote Sens. Environ.*, vol. 262, 2021, Art. no. 112499, doi: 10.1016/j.rse.2021.112499.
[23] D. Hong, N. Yokoya, J. Chanussot, and X. X. Zhu, "An augmented linear mixing model to address spectral variability for hyperspectral unmixing," *IEEE Trans. Image Process.*, vol. 28, no. 4, pp. 1923–1938, Apr. 2019, doi: 10.1109/TIP.2018.2878958.
[24] S. Yamamoto, S. Tsuchida, M. Urai, H. Mizuochi, K. Iwao, and A. Iwasaki, "Initial analysis of spectral smile calibration of hyperspectral imager suite (HISUI) using atmospheric absorption bands," *IEEE Trans. Geosci. Remote Sens.*, vol. 60, 2022, Art. no. 5534215, doi: 10.1109/TGRS.2022.3190486.
[25] M. Meroni et al., "Characterization of fine resolution field spectrometers using solar Fraunhofer lines and atmospheric absorption features," *Appl. Opt.*, vol. 49, no. 15, pp. 2858–2871, 2010, doi: 10.1364/AO.49.002858.
[26] K. Obata et al., "An overview of ISS HISUI hyperspectral imager radiometric calibration," in *Proc. IEEE Int. Geosci. Remote Sens. Symp.*, 2016, pp. 1924–1927, doi: 10.1109/IGARSS.2016.7729495.
[27] D. R. Thompson et al., "Imaging spectrometer stray spectral response: In-flight characterization, correction, and validation," *Remote Sens. Environ.*, vol. 204, pp. 850–860, 2018, doi: 10.1016/j.rse.2017.09.015.
[28] S. Yamamoto, H. Mizuochi, M. Matsuoka, K. Iwao, and S. Tsuchida, "Analysis based on onboard lamp and lunar vicarious calibrations for sensitivity degradation of a hyperspectral sensor," *IEEE Trans. Geosci. Remote Sens.*, vol. 60, 2022, Art. no. 4601212, doi: 10.1109/TGRS.2021.3127163.
[29] RadCalNet. Accessed: Feb. 29, 2024. [Online]. Available: https://www.radcalnet.org/#!/
[30] PICS. Accessed: Feb. 29, 2024. [Online]. Available: https://https://picscar.magellium.com
[31] R. Richter, D. Schlapfer, and A. Müller, "Operational atmospheric correction for imaging spectrometers accounting for the smile effect," *IEEE Trans. Geosci. Remote Sens.*, vol. 49, no. 5, pp. 1772–1780, May 2011, doi: 10.1109/TGRS.2010.2089799.

Satoru Yamamoto received the Ph.D. degree in science from Kobe University, Kobe, Japan, in 1999.

He is currently a Group Leader with the Research Institute of Geology and Geoinformation, Geological Survey of Japan, National Institute of Advanced Industrial Science and Technology, Tsukuba, Japan. He is involved in the Earth observation remote-sensing projects of ASTER and HISUI and the Lunar Mission Project of SELENE/Kaguya.

Dr. Yamamoto is a Member of the Japanese Society of Planetary Sciences, the Japan Geoscience Union, and the Remote Sensing Society of Japan.

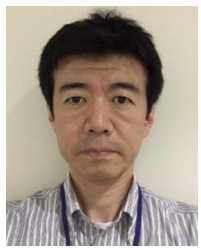

Satoshi Tsuchida received the B.S. degree in geology and the Ph.D. degree in mineral resources engineering from Waseda University, Tokyo, Japan, in 1986 and 1991, respectively.

He joined the Geological Survey of Japan (GSJ) in 1992 to engage in research in geological and environmental remote sensing and calibration of radiometers on satellites. He is currently an invited senior Researcher with the GSJ, National Institute of Advanced Industrial Science and Technology, Tsukuba, Japan.

Minoru Urai received the Ph.D. degree in science from Kagoshima University, Kagoshima, Japan, in 2004.

In 1981, he joined the Geological Survey of Japan, where he was engaged in research on volcano observation using remote sensing. He moved to the National Institute of Advanced Industrial Science and Technology (AIST), into which the Geological Survey of Japan and 15 other national institutes were reorganized in 2001. He joined Japan Space Systems in 2021. He has been a Collaborating Visitor with AIST since 2021.

Hiroki Mizuochi received the Ph.D. degree in environmental studies from the University of Tsukuba, Tsukuba, Japan, in 2017.

He is currently a Researcher with the Geological Survey of Japan, National Institute of Advanced Industrial Science and Technology, Tokyo, Japan, a Visiting Associate Professor with ISEE, Nagoya University, Nagoya, Japan, and a Visiting Associate Professor with the Graduate School of Frontier Sciences, the University of Tokyo, Tokyo, Japan. He is involved in the Earth observation remote-sensing projects of ASTER and HISUI, and Pan-Arctic Water-Carbon Cycles JSPS scientific research.

Dr. Mizuochi is a Member of the Remote Sensing Society of Japan, the Japan Society of Photogrammetry and Remote Sensing, and the Japan Geoscience Union.

Moe Matsuoka received the Ph.D. degree in science from Tohoku University, Sendai, Japan, in 2018.

She is currently a Researcher with the Research Institute of Geology and Geoinformation, Geological Survey of Japan, National Institute of Advanced Industrial Science and Technology, Tsukuba, Japan. She is involved in the Earth observation remote-sensing projects of ASTER and HISUI, the asteroid exploration missions of Hayabusa 2, and MMX.

Dr. Matsuoka is a Member of the Japanese Society of Planetary Sciences.

Koki Iwao received the Ph.D. degree in engineering from the University of Tokyo, Tokyo, Japan, in 2000.

He is currently a Researcher with the Research Institute of Geology and Geoinformation, Geological Survey of Japan, Institute of Advanced Industrial Science and Technology, Tsukuba, Japan. He is involved in the Earth observation remote-sensing projects of ASTER and HISUI.

Dr. Iwao is a Member of the Remote Sensing Society of Japan, the Japan Society of Photogrammetry and Remote Sensing, and the Japan Association of Surveyors.